



Microstructures, Mechanical and High-Temperature Tribological Properties of Dual-Phase Fe₅₀Mn₃₀Co₁₀Cr₁₀ High-Entropy Alloy Fabricated by Laser Metal Deposition

MING SUN,^{1,2} GUOCHENG LIU ^{1,2,3} WENTING WEI,^{1,2}
LINGYUN ZHOU,^{1,2} JIANJIANG LI,^{1,2} and QIYONG TU^{1,2}

1.—Hubei Key Laboratory of Advanced Technology for Automotive Components, Wuhan University of Technology, Wuhan 430070, China. 2.—Hubei Collaborative Innovation Center for Automotive Components Technology, Wuhan University of Technology, Wuhan 430070, China. 3.—e-mail: liugch@whut.edu.cn

The dual-phase Fe₅₀Mn₃₀Co₁₀Cr₁₀ (atomic percent, at.%) high-entropy alloy (HEA) was fabricated successfully through a laser metal deposition process. Fe₅₀Mn₃₀Co₁₀Cr₁₀ HEA consisted of face-centered cubic (FCC) γ and hexagonal close-packed (HCP) ϵ phases, with an alternating distribution of equiaxed and columnar grains. The microhardness, tensile strength and elongation of the alloy were 270 ± 20 HV, 689 MPa and 38%, respectively. After tensile deformation, many HCP ϵ phases were generated inside and at the boundaries of FCC γ grains because of the transformation-induced plasticity effect. The content of the HCP ϵ phase increased because of tensile deformation, resulting in a 75% decrease in the average grain size of the samples. Under the effect of dispersion strengthening, the strength, microhardness and plasticity of the material were greatly enhanced, with the product of strength and elongation up to 26.2 GPa%. The average friction coefficient and wear rate of the alloy were 0.43 and 1.88×10^{-5} mm³/N/m at 400°C, respectively, which were 38.6% and 81.6% lower than those at room temperature, showing great high-temperature wear resistance. The main wear mechanism of the alloy at 400°C was oxidative wear, accompanied by abrasive wear and delamination.

INTRODUCTION

To obtain new materials with superior properties, people are constantly developing new alloys. In recent years, high-entropy alloy (HEA) consisting of multiple principal elements has attracted interest in research and application.^{1–6} HEA was originally defined as a single-phase solid solution containing at least five principal elements and the concentration of each principal element ranged between 5 and 35 atomic percent (at.%). However, with the development of research, component design from the perspective of configuration entropy becomes a more prominent feature of HEA. Due to the characteristics of multiple principal elements, HEA exhibits

unique structure and outstanding properties, such as excellent hardness and strength,^{7–9} superior high elongation,^{10,11} great wear resistance^{12,13} and unique corrosion resistance,¹⁴ which gives it broader application prospects in the fields of biology and aviation compared with traditional alloys.

In the original HEA design concept, guided by the principle of maximum configurational entropy, phase separation was not expected because it indicated the instability of the state of a single solid solution. In this case, previous studies focused more on single-phase equiatomic HEA. However, many studies reflected the fact that single-phase equiatomic HEA does not necessarily exhibit excellent properties. The current studies are no longer limited to entropy-stabilized single-phase equiatomic HEA. The development of multi-phase and non-equiatomic HEA has become an important research direction.^{15–18} Recently, Li et al.^{19,20} developed a

(Received January 24, 2023; accepted March 13, 2023;
published online April 5, 2023)

new class of transformation-induced plasticity-assisted dual-phase high-entropy alloy (TRIP-DP-HEA), which consisted of two high-entropy phases [i.e., face-centered cubic (FCC) γ and hexagonal close-packed (HCP) ϵ phases]. The TRIP-DP-HEA exhibits high ultimate tensile strength and elongation through massive solid solution strengthening and phase transformation-induced hardening and overcomes the strength-ductility trade-off.

Arc melting^{17,21} and induction melting^{19,22} are commonly used to fabricate HEA bulk samples at present. However, coarse grains and component segregation caused by the above processes set a limit to the performance and application of HEA. Fortunately, additive manufacturing (AM) provides a powerful solution to solve the problems existing in traditional manufacturing processes. AM technology has the characteristics of flexibility and agility and can realize the integration of material manufacturing and shaping. Laser metal deposition (LMD) is a method that combines traditional rapid prototyping and laser cladding technology. Besides, the LMD process is characterized by a high solidification rate of 10^4 – 10^6 K/s,²³ which provides the possibility to fabricate HEA samples with fine grains and homogeneous compositions. According to existing reports, there have been some studies using the LMD process to prepare HEA, and good results have been obtained.^{24–27} Niu et al.²⁸ fabricated Fe₅₀Mn₃₀Co₁₀Cr₁₀ (at.%) using the LMD process, and the results indicated that Fe₅₀Mn₃₀Co₁₀Cr₁₀ with excellent mechanical properties was successfully produced by the LMD technique, with the anisotropic mechanical properties of the material observed. However, there is less research on the fabrication of Fe₅₀Mn₃₀Co₁₀Cr₁₀ by the LMD process, and the understanding of its microstructures and properties is still incomplete. Therefore, it is of great significance to carry out relevant research.

In this study, the coaxial powder feeding LMD technique was used to fabricate dual-phase Fe₅₀Mn₃₀Co₁₀Cr₁₀ HEA thin-wall samples with the study of microstructure characteristics, phase component and structural evolution due to plastic deformation. The mechanical and tribological properties of HEA samples were tested and the wear mechanisms at high temperatures were also analyzed.

EXPERIMENTAL

The Fe₅₀Mn₃₀Co₁₀Cr₁₀ powders with particle sizes 45–105 μm were produced by gas atomization of Fe, Mn, Co and Cr (99.99% purity) in Ar atmosphere. The chemical composition of the powders (Fe: 49.86 at.%, Mn: 29.81 at.%, Co: 10.65 at.%, Cr: 9.68 at.%) was near to the nominal composition. AISI 316 stainless steel plates were used as substrate materials. The laser system used for the experiments was a YLS-2000-S2T fiber laser with a wavelength of 1070 nm. The powder was delivered

by coaxial blown powder equipment at a rate of 3 g/min with argon carrier gas at a flow rate of 20 l/min. Argon shielding gas with a flow rate of 20 l/min is used at the bottom of the nozzle to protect the laser optics. During the deposition process, the environment in the working chamber was isolated from the atmosphere and continuously filled with high-purity argon gas to ensure a low oxygen atmosphere in the working chamber (< 100 ppm). After many experiments on parameter optimization, the LMD process parameters are selected as follows: laser power was 500 W, laser beam diameter was 1.2 mm and scanning speed was 200 mm/min. The samples were deposited using the single-track and multi-layer strategy. The height of the laser head rose by 0.5 mm after each single-track scan.

The phase analysis was examined by X-ray diffraction (XRD) with Cu-K α radiation ($\lambda = 0.15406$ nm) at 40 kV and 40 mA. The samples were scanned over a scattering angle range of $30^\circ < 2\theta < 110^\circ$ with a scanning speed of $4^\circ/\text{min}$. The microstructural characterization of the samples was observed by optical microscope (OM) and scanning electron microscope (SEM). X-ray energy dispersive spectrometer (EDS) was used to analyze the chemical composition and element segregation. The phase distribution, grain size and crystal orientation were characterized using electron backscatter diffraction (EBSD). The tensile property was performed at room temperature using a universal Instron-5967 testing system with a strain rate of 10^{-3} s⁻¹. The hardness of the samples was measured 20 times at an interval of 0.5 mm by a Vickers microhardness tester with a load of 1.96 N (200 g) and a loading time of 15 s, and the average and standard deviation values were calculated. The wear-resistance test was carried out in HT-1000 high-temperature friction and wear tester in the temperature range of 25–400°C with a friction velocity of 700 r/min, friction radius of 5 mm and loading of 19.6 N (2000 g) for 60 min. Si₃N₄ balls were used as the friction pairs. The wear trace morphology and chemical component were analyzed by MicroXAM-800 type white-light interferometer, SEM and EDS. X-ray photoelectron spectroscopy (XPS) was conducted to examine the chemical states of different elements on the worn surface. The density of the alloy was calculated by Archimedes' principle using the following formula:

$$\rho = \frac{m_1}{m_1 - m_2} \rho_0 \quad (1)$$

where ρ is the density of the alloy (g/cm³), m_1 is the weight of a dry alloy block measured in the air (g), m_2 is the weight of the same alloy block measured in water (g), and ρ_0 is the density of water (g/cm³). The wear rate of the alloy was calculated using the following formula:

$$\delta = \frac{V}{N \cdot d} \quad (2)$$

where δ is the wear rate of the alloy ($\text{mm}^3/\text{N/m}$), V is the volume loss of the alloy after the wear test (mm^3), N is the load applied during the wear test (N), and d is the sliding distance of the grinding ball on the alloy surface during the wear test (m).

RESULTS

Mechanical Properties

Typical mechanical properties of $\text{Fe}_{50}\text{Mn}_{30}\text{Co}_{10}\text{Cr}_{10}$ HEA are shown in Fig. 1. Figure 1a presents the microhardness of LMD samples in different states. The microhardness of the as-deposited samples is 270 ± 20 HV, similar to the result for $\text{Fe}_{50}\text{Mn}_{30}\text{Co}_{10}\text{Cr}_{10}$ HEA fabricated using arc melting.²⁹ In addition, compared with the results of the as-deposited samples, the microhardness of deformed samples near the fracture significantly increases to 324 ± 16 HV. This is attributed to the higher microhardness of the HCP phase compared to the FCC phase. The HCP phase obtained from martensitic transformation is the

key to improving the microhardness of deformed specimens.

Figure 1b presents the engineering stress–strain curves at room temperature (25°C, RT) of $\text{Fe}_{50}\text{Mn}_{30}\text{Co}_{10}\text{Cr}_{10}$ HEA specimens produced using different processing. The ultimate tensile strength and elongation of LMD HEA samples are 689 MPa and 38%, respectively. LMD samples exhibit excellent comprehensive strength-ductility properties compared with the samples fabricated by other processes.^{30–32} However, compared with the coarse-grained (about 45 μm grain size) samples produced in a vacuum induction furnace,¹⁹ the ultimate tensile strength of LMD samples is close, but the elongation is poor. This can be attributed to the effect of post-treatment. Previous studies have shown that the mechanical properties of HEA can be improved by post-treatment.^{33,34} The sample in this work is in the as-deposited state. However, the as-cast samples were hot-rolled and homogenized at high temperatures by Li et al.,¹⁹ which contributed to the improvement of the mechanical properties. Figure 1c reveals the true stress–strain curve and

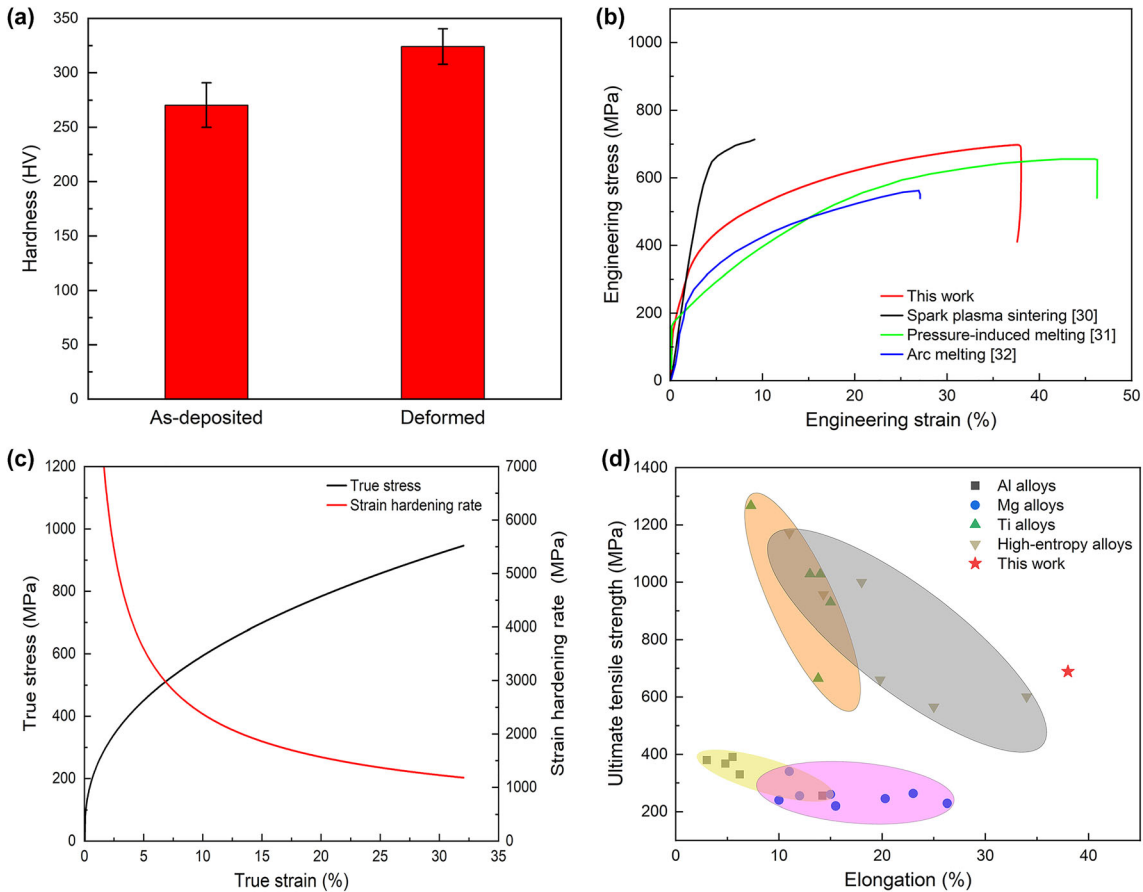


Fig. 1. Typical mechanical properties of $\text{Fe}_{50}\text{Mn}_{30}\text{Co}_{10}\text{Cr}_{10}$ HEA: (a) Vickers microhardness of the alloy in different states; (b) engineering stress–strain curves of $\text{Fe}_{50}\text{Mn}_{30}\text{Co}_{10}\text{Cr}_{10}$ HEA fabricated by different techniques; (c) true stress–strain and corresponding strain-hardening rate–true strain curves of $\text{Fe}_{50}\text{Mn}_{30}\text{Co}_{10}\text{Cr}_{10}$ HEA; (d) relationship between the ultimate tensile strength and elongation of Al alloys (AlSi10Mg,^{35,36} Al-5Si,³⁷ Al-12Si^{38,39}), Mg alloys (Mg-1.5Mn,⁴⁰ Mg-1.5Al-0.2Zn-0.2Mn,⁴⁰ Mg-6Zn-0.5Zr,⁴⁰ Mg-0.3Al-0.21Ca-0.47Mn,⁴¹ Mg-2.97Al-0.8Zn-0.36Mn,⁴¹ AZ31^{40,42}), Ti alloys (Ti-6Al-4 V,^{43–46} Ti-24Nb-4Zr-8Sn⁴⁷), HEAs (AlCoCrFeNi_{2.1},⁴⁸ Al_{0.7}CoCrFeNi,²⁸ AlCoCuFeNi_{3.0},⁴⁹ CoCrFeMnNi^{24,50,51}) and present work at RT.

the corresponding work-hardening rate curve of LMD HEA specimens. LMD samples exhibit a prominent work-hardening ability at high strain levels because of the transformation-induced plasticity (TRIP) effect.

Figure 1d shows the ultimate tensile strength and elongation of various alloys at room temperature.^{35–51} Al, Mg and Ti alloys are widely used because of their outstanding strength or plasticity.^{52–54} However, conventional alloys are limited in the trade-off between strength and ductility. In contrast, HEA with multiple principal elements shows excellent strength-plasticity properties due to the complexity and uniqueness of chemical compositions, while Fe₅₀Mn₃₀Co₁₀Cr₁₀ HEA with the TRIP effect exhibits more outstanding performance. Compared with Al, Mg and Ti alloys, the remarkable strength-ductility properties of HEA make it perform better in the product of strength and elongation, which is up to 26.2 GPa%. Based on this, LMD Fe₅₀Mn₃₀Co₁₀Cr₁₀ HEA has promising potential for use in engineering applications.

Figure 2a presents the macroscopic morphology of tensile fracture. It can be seen that the fracture surface is uneven, fibrous and dark in color, reflecting the overall morphology of ductile fracture. Figure 2b shows the microstructures of the central area of the fracture surface. Holes and dimples are observed on the fracture surface, and there are also deep and large dimples, which indicate the good plasticity of LMD HEA samples. Besides, many second-phase particles are found at the bottom of the dimples, and these particles can be used as the core of the micropore nucleation, further confirming that a ductile fracture with micropore aggregation is the main fracture mode. Dimples are surrounded by short, curved and fibrous tearing edges (bright white) that help absorb more energy and increase the elongation of the samples.

Phase Component and Microstructure

Figure 3a presents the XRD patterns of the as-deposited and deformed Fe₅₀Mn₃₀Co₁₀Cr₁₀ HEA. The as-deposited Fe₅₀Mn₃₀Co₁₀Cr₁₀ HEA consists of two phases: FCC γ and HCP ϵ phases, consistent with the results reported by Li et al.¹⁹ Noticeably, after tensile deformation, the intensity of the diffraction peak of the FCC γ phase decreases, while that of the HCP ϵ phase increases. These results indicate that the metastable FCC γ phase undergoes a martensite transformation from FCC γ to the HCP ϵ phase during the tensile deformation.

Figure 3b shows the metallographic structure of LMD HEA in the scanning direction-building direction (SD-BD) section. The single-track deposition layer boundary along the scanning direction can be observed. The height of the single-track deposition layer is approximately 0.5 mm. The samples consist of equiaxed and columnar grains. Besides, it is observed that equiaxed grains are mainly distributed in the molten pool. The columnar grains are arranged roughly parallel to the direction of deposition and pass through multiple deposition layers. Notably, a few pores are found in the SD-BD section, which may be caused by gas retention in the molten pool during LMD processing.

Figure 4 shows the microstructure and elemental distribution of LMD HEA in the SD-BD section at a smaller scale. In the undeformed state, a small amount of granular HCP ϵ phase can be observed in the FCC γ matrix. The HCP ϵ phase was removed from the FCC γ matrix etched by FeCl₃ solution so that the morphology of the HCP ϵ phase could be observed. After tensile deformation, due to a strain-induced martensite transformation, the metastable FCC γ phase undergoes the transition from the FCC γ phase to the HCP ϵ phase as a primary deformation mechanism, which is consistent with previous research.^{19,55} Moreover, EDS maps (Fig. 4c) indicate that all the elements, i.e.,

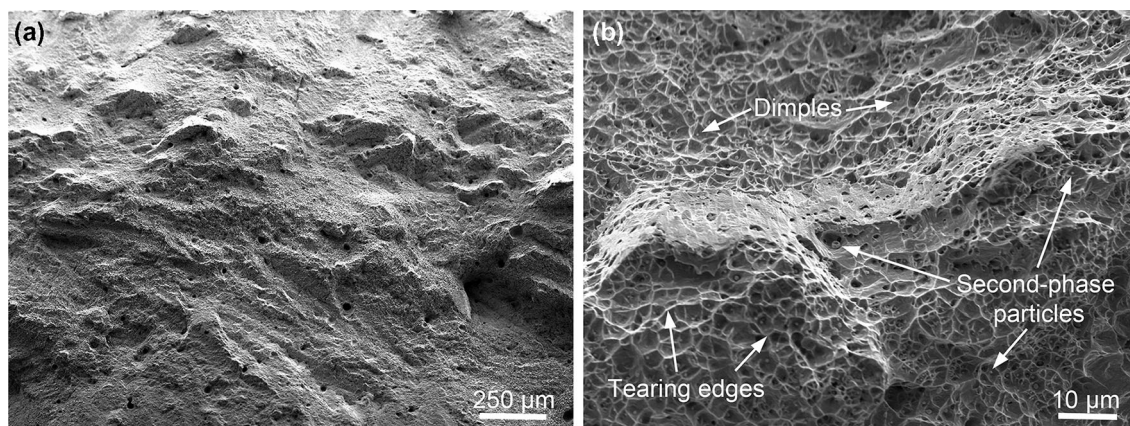


Fig. 2. SEM images of fracture morphology of the tensile specimens at: (a) low magnification; (b) high magnification.

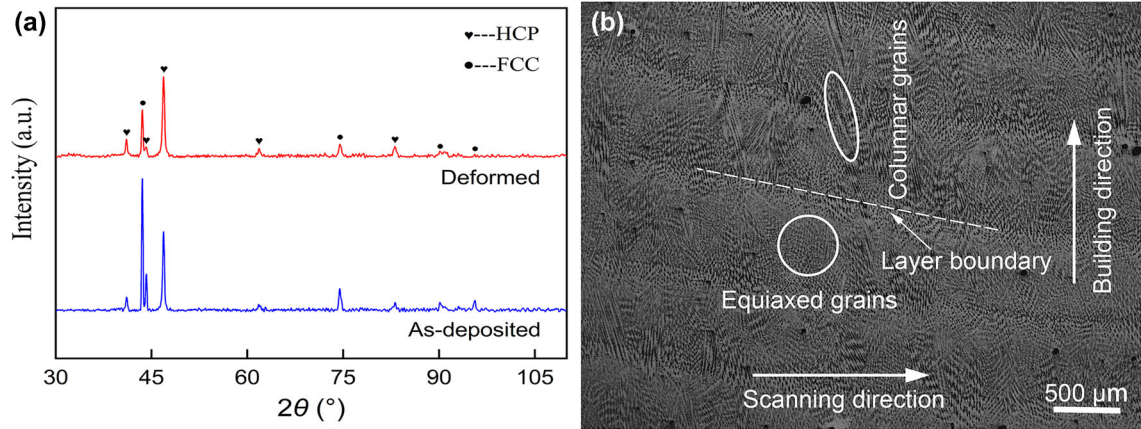


Fig. 3. Phase component and microstructure of $\text{Fe}_{50}\text{Mn}_{30}\text{Co}_{10}\text{Cr}_{10}$ HEA: (a) XRD patterns in different states; (b) OM image of the as-deposited alloy.

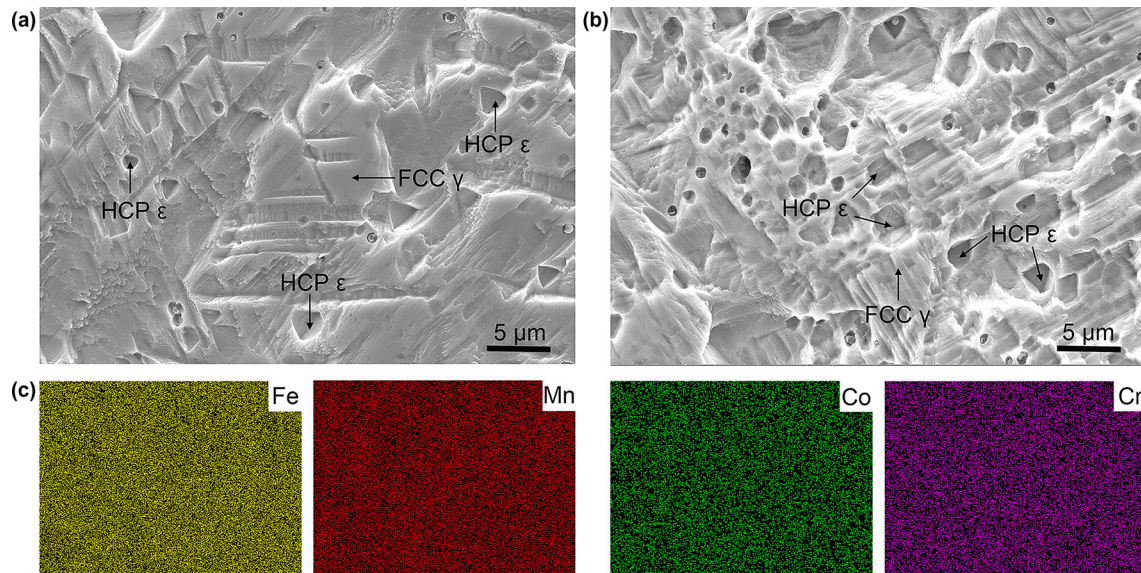


Fig. 4. Microstructures and element distributions of LMD HEA on the SD-BD cross-section: (a) in the undeformed state; (b) after the deformation; (c) EDS map corresponding to the region in (a).

Fe, Mn, Co and Cr, are evenly distributed at the grain scale in dual-phase HEA, and no component segregation is detected.

Figure 5 presents the EBSD images of LMD HEA specimens. The phase distributions in the middle region of the as-deposited specimens and near the fracture of the deformed specimens are shown in Fig. 5a and b. According to the phase distribution maps, the area fraction of the FCC γ phase of the as-deposited sample is about 88.7%, and the rest is HCP ϵ phase, about 11.3%. After tensile deformation, the area fraction of the FCC γ phase decreases to 71.3%, and the area fraction of the HCP ϵ phase increases to 28.7%, indicating the transition from the FCC γ phase to the HCP ϵ phase, which is also consistent with XRD results. Figure 5c and d shows the statistical results of the grain size distribution of LMD HEA in an as-deposited and deformed state, respectively. The maximum and average

grain size of the HEA in the undeformed stage is about $120\ \mu\text{m}$ and $67\ \mu\text{m}$, respectively. Combined with Fig. 5a, it is seen that all the large-size grains are FCC γ phase, while most of the small-size grains are HCP ϵ phase. The maximum and average grain size of the deformed HEA is greatly reduced to about $80\ \mu\text{m}$ and $17\ \mu\text{m}$, respectively. The decrease in the average grain size is attributed to the fragmentation, twin and phase transition of FCC γ grains under stress and the increase of the proportion of small-size HCP ϵ phase, as shown in Fig. 5b. Noticeably, initial HCP ϵ grains (of about $3\ \mu\text{m}$ grain size) in HEA mostly exist in FCC γ grains, while new HCP ϵ grains appear both inside and at the boundaries of FCC γ grains. Figure 5e and f shows the grain orientation of the alloy in the normal direction (ND) and loading direction (LD). FCC γ large grains of the as-deposited samples show mainly two orientation components

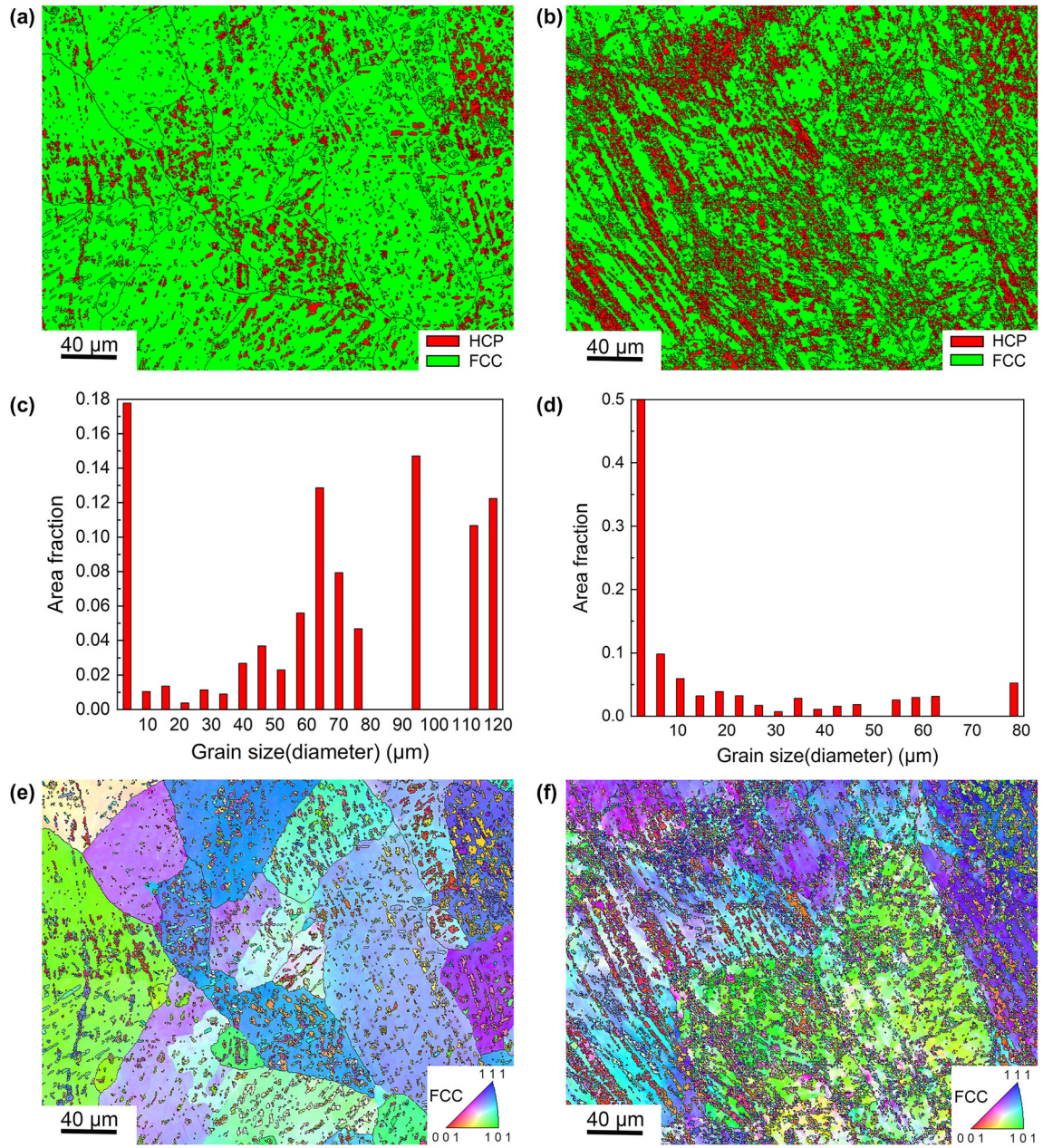


Fig. 5. Phase maps, grain size distributions and inverse pole figure maps of Fe₅₀Mn₃₀Co₁₀Cr₁₀ HEA on the SD-BD cross-section: (a, c, e) as-deposited; (b, d, f) deformed.

(Fig. 5e), $\langle 101 \rangle // ND$ (green) and close to $\langle 111 \rangle // ND$ (blue and purple), consistent with the results of cold-rolled Fe_{49.5}Mn₃₀Co₁₀Cr₁₀C_{0.5} HEA after tempering.⁵⁶ After tensile deformation, FCC γ large grains show obvious $\langle 101 \rangle // LD$ and close to $\langle 111 \rangle // LD$ orientation (Fig. 5f).

Tribological Properties

Figure 6a shows the variation curves of the friction coefficient for LMD HEA samples under different wear test temperatures. The friction

coefficient of the samples is low in the initial stage because of the breaking-in process between the samples and the grinding ball. After a 5–10 min wear test, the friction coefficient increases gradually, and then the samples reach a steady wear stage. Notice that the friction coefficient curves present a typical phenomenon of sawtooth fluctuation. However, the difference lies in the fluctuation degree of each sample curve. Besides, the value of the friction coefficient for the samples under different test temperatures in the steady state is given in Table I. The average friction coefficient of the

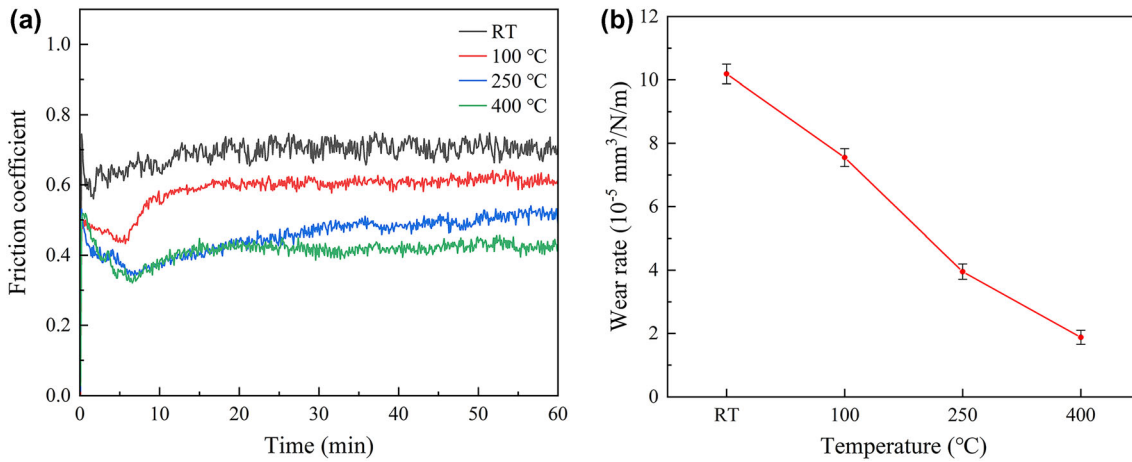


Fig. 6. Tribological properties of $\text{Fe}_{50}\text{Mn}_{30}\text{Co}_{10}\text{Cr}_{10}$ HEA at different temperatures: (a) friction coefficient versus time curves; (b) wear rate.

Table I. Friction coefficient of $\text{Fe}_{50}\text{Mn}_{30}\text{Co}_{10}\text{Cr}_{10}$ HEA in the steady state.

Temperature (°C)	Friction coefficient
RT	0.70 ± 0.05
100	0.59 ± 0.03
250	0.51 ± 0.04
400	0.43 ± 0.03

samples decreases with the increase of wear test temperature and decreases by 38.6% at 400°C compared with at RT. Figure 6b shows the wear rate of the samples at different test temperatures. Like the changing trend of the friction coefficient, the wear rate of all samples also decreases with the increase of test temperature, indicating that LMD HEA exhibits more excellent wear resistance at high temperatures.

Figure 7a shows the wear track profiles at different temperatures. The depth and width of the wear track both decrease with the increase in the test temperature. At the highest temperature of 400°C, the depth and width of the wear track are 32.1 μm and 1220.5 μm , respectively. The decrease in the depth and width of the wear track indicates a decrease in the volume loss, and the wear rate of the alloy is the lowest when the volume loss is the smallest. In addition, the hardness of the alloys tested at different temperatures was measured, as shown in Fig. 7b. Obviously, the hardness of the alloy increases as the test temperature increases. This is attributed to the local plastic deformation and high-temperature oxidation mechanism of the alloy during the wear tests, and the fine-grain HCP ϵ phase is induced by the FCC γ phase under the action of stress, which increases the content of the HCP ϵ phase with higher hardness. The increase in the hardness of the alloy is conducive to obtaining better wear resistance, thus leading to a decrease in the wear rate.

DISCUSSION

Microstructure Characteristics of the LMD HEA

The LMD samples have the microstructure characteristics of equiaxed and columnar grains, which can be attributed to the variation in the temperature gradient (G) and the solidification rate (R).⁵⁷ The formation of grain morphology during the LMD process is shown in Fig. 8. When the laser scans a single track on the substrate, there is a higher temperature gradient and faster solidification rate at the bottom of the molten pool in contact with the substrate due to the high energy of the laser beam, which promotes the formation of columnar grains with the growth direction parallel to the direction of the maximum thermal gradient at the bottom of the molten pool. Meanwhile, it is easier to form equiaxed grains on the top of the molten pool because of a smaller temperature gradient. When a new layer is deposited on the previous layer, equiaxed grains on the top of the previous layer are partly remelted, providing nuclei for the formation of columnar grains. As the deposition height increases, the previously deposited layers gradually cool to a relatively lower temperature, while the newly deposited layer has a higher temperature due to the high laser beam energy. Therefore, a large temperature gradient is generated along the deposition direction, and the existence of the temperature gradient promotes the growth of columnar grains along the deposition direction. Because of this, columnar grains typically pass through multiple deposition layers. With the progress of the solidification, the temperature gradient decreases and the solidification rate increases, which is beneficial to the occurrence of columnar to equiaxed transitions.⁵⁸

Previous studies have shown that process parameters such as scanning speed and laser power can affect the value of G and R .⁵⁹ Under the premise of constant scanning speed, increasing the laser power

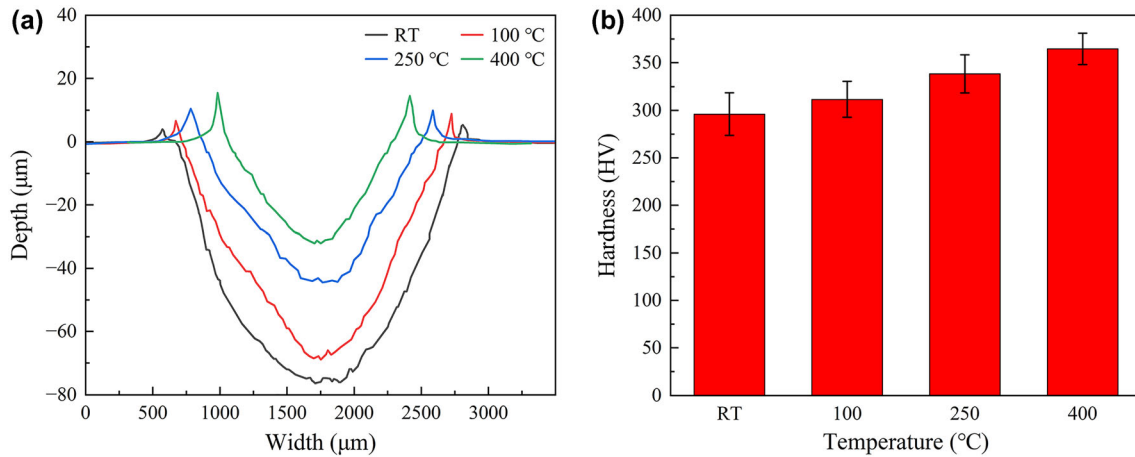


Fig. 7. Wear track morphology and hardness of HEA at different temperatures: (a) 2D cross-section profiles of the wear track; (b) Vickers hardness of the alloy.

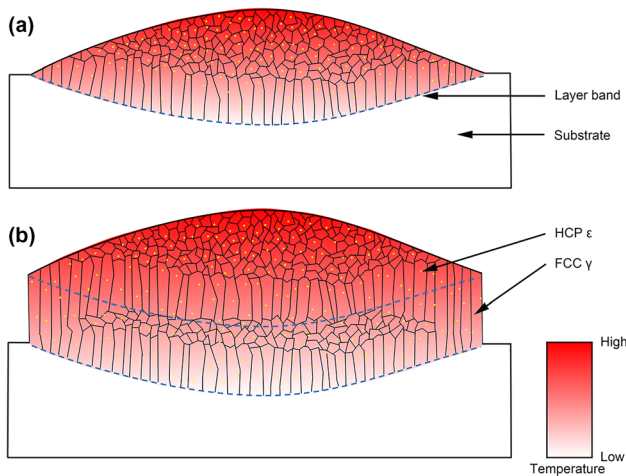


Fig. 8. Schematic illustration of the evolution of grains during the LMD process: (a) single-track; (b) multi-layer.

reduces both the temperature gradient and solidification speed, but the value of G/R decreases. Therefore, the grains tend to transform from columnar to equiaxed transformation. When the laser power is constant, decreasing the scanning speed is equivalent to increasing the incident energy, which causes the grains to transform from columnar to equiaxed. The variation of the temperature gradient and solidification rate caused by the LMD process parameters is the key factor to change the grain characteristics, and appropriate process parameters can effectively control the microstructures.

The grains of LMD samples are relatively fine (the average grain size is about 67 μm), and the fine grains provide more interfaces to hinder dislocation motion, which is beneficial to the high strength of the material. In addition, in the process of tensile deformation, many small-size HCP ε phases appear and disperse on the FCC γ matrix because of the TRIP effect, realizing the effect of dispersion

strengthening, which is one of the main reasons for the high strength of Fe₅₀Mn₃₀Co₁₀Cr₁₀ HEA fabricated by LMD process.

Formation Characteristics of Phase

Early research on TRIP steel found that the TRIP effect is mainly related to stacking fault energy.⁶⁰ The previous research confirmed that in the Fe_{80-x}Mn_xCo₁₀Cr₁₀ HEA system, only when the Mn content reached 30 at.% could the stacking fault energy in the FCC γ phase meet the requirements for realizing the TRIP effect, thereby forming the TRIP-DP-HEA.¹⁹ This also confirms the rationality of the above conclusion in the TRIP-DP-HEA. Many stacking faults in the FCC γ phase act as the core of the HCP ε phase nucleation, which can realize the transformation from the metastable FCC γ phase to the HCP ε phase when subjected to externally applied loads. This is also the main deformation mechanism of the HEA.

The grain boundaries are usually the main nucleation sites for phase transition, and the HCP ε phase is believed to be more likely to nucleate and grow at the FCC grain boundaries.⁶¹ The EBSD results show that the HCP ε phase mostly exists in the FCC γ grains in the undeformed stage. After tensile deformation, the nucleation of the transition from the FCC γ phase to the HCP ε phase is easier because of the increase in grain boundary area caused by the decrease in FCC grain size. Therefore, a large amount of newly added HCP ε phase can be found at the FCC γ grain boundaries. As the deformation progresses, multiple deformation mechanisms (i.e., dislocation slip, twinning and stacking fault formation) are also activated in the HCP ε phase, which plays an important regulating role in the uniform plastic deformation and strain-hardening of the specimens. In addition, the growth of the transformed HCP ε phase is limited by grain boundaries. Notably, the HCP ε phase in LMD HEA

is granular, as shown in Fig. 4a, which is different from the previous lath shape and possibly due to the unique single-track and multi-layer fabrication strategy of the LMD process. As shown in Fig. 8, granular HCP grains with high microhardness are dispersed in the interior and boundary of FCC grains, forming a pinning effect, which can greatly improve the comprehensive strength of LMD samples.

Wear Mechanisms of Fe₅₀Mn₃₀Co₁₀Cr₁₀ HEA

To better understand the wear mechanisms of Fe₅₀Mn₃₀Co₁₀Cr₁₀ HEA at different temperatures, SEM and EDS analyses of the worn surfaces of the samples after wear tests at RT and 400°C were performed, as shown in Fig. 9 and Table II. The worn surface characteristics of the samples at RT and 400°C are quite similar, and multiple wear mechanisms can be observed simultaneously. According to the EDS analysis of the worn surfaces (Table II), the areas where point B and E were located are oxide layers, which confirms the occurrence of oxidative wear during the wear tests and also explains why the friction coefficient curve exhibits typical sawtooth fluctuations in the steady stage. This is because when a protective oxide layer with higher hardness is formed on the worn

surfaces of the samples, the direct contact between the samples and the Si₃N₄ balls is isolated, resulting in a decrease in the friction coefficient. However, within a short period, the oxide layer is broken, the worn surfaces are in direct contact with the Si₃N₄ balls, and the friction coefficient increases. During the steady wear phase, the above process is constantly repeated. The degree of oxidation of the worn surfaces that are not in contact with the Si₃N₄ balls is more severe at high temperatures than at RT by comparing the compositions of point C and F. Meanwhile, the oxide layer formed at RT was discontinuous, and the area of the oxide layer on the worn surfaces gradually increased with the

Table II. Chemical composition inside the wear tracks of the HEA samples (at.%)

Element	Fe	Mn	Co	Cr	Si	O
A	26.55	16.66	5.60	5.92	0.78	44.49
B	17.43	10.47	3.75	3.80	1.32	63.23
C	46.09	26.69	9.31	9.59	0.00	8.32
D	17.48	10.63	3.73	3.69	0.76	63.71
E	20.69	12.37	4.38	4.48	0.77	57.31
F	36.65	21.68	7.69	7.40	0.00	26.58

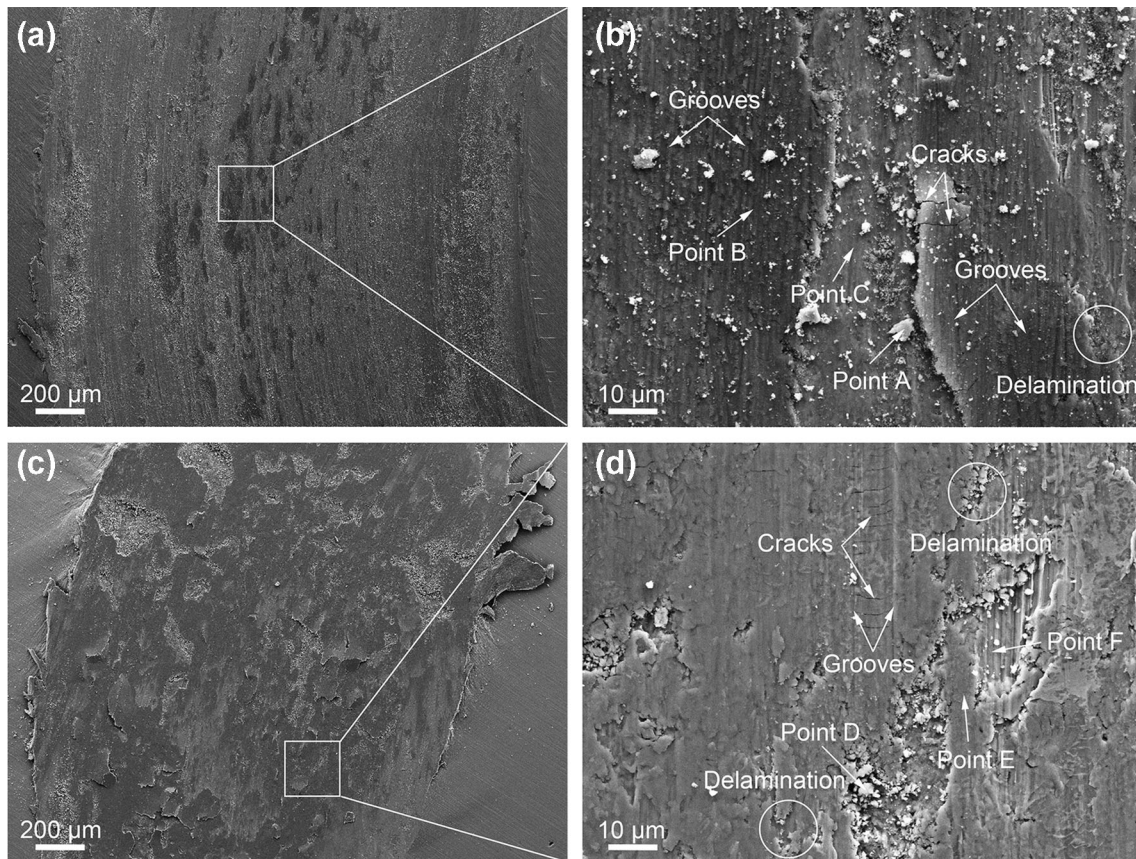


Fig. 9. SEM images of the worn surfaces of HEA specimens at: (a, b) RT; (c, d) 400°C. (a) and (c) Morphologies of the worn surfaces at low magnification and (b) and (d) magnified morphologies corresponding to the identical regions marked in (a) and (c).

increase of the test temperature. In addition, there is no significant difference between the proportion of each element in white particles and the oxide layers by comparing the composition of white particles corresponding to point A and point D with that of the oxide layer, which indicates that the particles fell off the oxide layers. In contrast, there were more white particles inside the wear tracks of the samples tested at RT, which indicates that the rupture degree of the oxide layers is greater. The increase of the area and integrity of the oxide layer at high temperatures can explain the decrease in the depth and width of the wear track as the test temperature increases and is also the key reason for the lower wear rate of the alloy at high temperatures.

To further investigate the chemical valence of different elements of the oxide layers, XPS tests were carried out on the worn surface of the samples after the wear test at 400°C, as shown in Fig. 10. In the Fe 2p spectrum (Fig. 10a), two pairs of peaks located at 712.6 eV (Fe 2p_{3/2}) and 726.0 eV (Fe 2p_{1/2}) are related with Fe³⁺, and the others peaks are

shakeup satellites (denoted as “Sat.”).^{62,63} The Mn 2p spectrum (Fig. 10b) shows the peaks at 642.5 eV (Mn 2p_{3/2}) and 654.0 eV (Mn 2p_{1/2}), indicating the coexistence of Mn²⁺ and Mn³⁺.^{62,64} In Fig. 10c, the peaks at 780.6 eV (Co 2p_{3/2}) and 796.3 eV (Co 2p_{1/2}) match with Co³⁺, while the peaks at 782.2 eV (Co 2p_{3/2}) and 797.6 eV (Co 2p_{1/2}) are related to Co²⁺.⁶⁵ Fig. 10d exhibits the peaks at a Cr 2p_{3/2} peak at 576.3 eV and a Cr 2p_{1/2} peak at 586.0 eV, suggesting the coexistence of Cr³⁺.⁶⁶ According to the XPS analysis, the oxide layer consists of Fe₂O₃, MnO, Mn₂O₃, CoO, Co₂O₃ and Cr₂O₃, and these substances work together to prevent direct contact between the alloy surface and the Si₃N₄ balls, thus improving the wear resistance of the alloy.

The morphologies of the wear tracks obtained at different temperatures all revealed the existence of ploughing grooves, which illustrates that abrasive wear is also one of the important wear mechanisms. According to the previous microhardness test, the difference in the microhardness between the Si₃N₄ balls and HEA samples is large, leading the harder

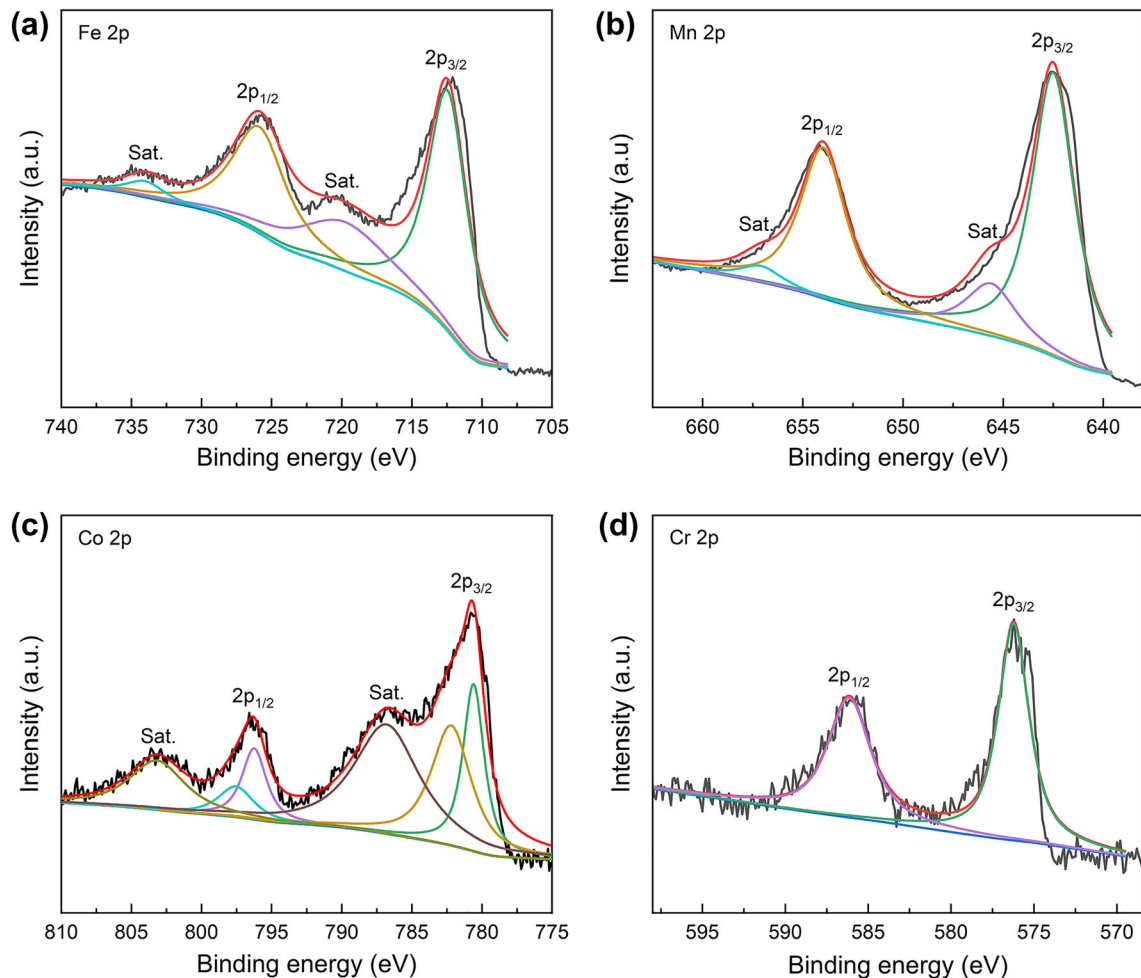


Fig. 10. XPS narrow spectra of the worn surface for HEA at 400°C: (a) Fe 2p; (b) Mn 2p; (c) Co 2p; (d) Cr 2p.

counter-abrasive material to slide easily on the softer surface of the samples and cause wear. Delamination and microcracks were also observed on the worn surfaces of the samples. The occurrence of delamination is attributed to the cold welding of worn particles to the surfaces after leaving the specimens. The appearance of cracks is due to the presence of the HCP ϵ phase as a primary phase of Fe₅₀Mn₃₀Co₁₀Cr₁₀ HEA. Meanwhile, the content of the HCP ϵ phase increases because of the TRIP effect during the wear tests, increasing the brittleness of the surfaces of samples to a certain extent and resulting in a decrease in the ability to inhibit the formation of cracks.

CONCLUSION

In this work, we successfully fabricated dual-phase Fe₅₀Mn₃₀Co₁₀Cr₁₀ HEA specimens with excellent performance using the LMD process based on coaxial powder feeding. The microstructure, phase composition, mechanical and tribological properties of the as-deposited samples were systematically investigated. The main conclusions are as follows:

- (1) The HEA samples fabricated using LMD consist of equiaxed and columnar grains because of the high temperature gradient and solidification rate of the laser processing. Besides, FCC γ and HCP ϵ phases were observed in the samples. During the plastic deformation, the metastable FCC γ phase transformed to the HCP ϵ phase because of the many stacking faults in the system, and both shared the strain.
- (2) The microhardness, ultimate tensile strength and elongation of the as-deposited samples are 270 ± 20 HV, 689 MPa and 38%, respectively. After tensile deformation, the TRIP effect occurred in the samples, with the HCP ϵ phase increased by 17.4%. The microhardness of the deformed samples increased by 20% due to the dispersion strengthening. The LMD Fe₅₀Mn₃₀Co₁₀Cr₁₀ HEA has excellent comprehensive strength-ductility properties compared with traditional alloys, showing the product of strength and elongation up to 26.2 GPa%.
- (3) The average friction coefficient and wear rate of LMD samples at RT are 0.70 and 1.02×10^{-4} mm³/N/m and decreased to 0.43 and 1.88×10^{-5} mm³/N/m when the test temperature increased to 400°C, respectively. With the increase of wear test temperature, the depth and width of the wear track both decrease, and the hardness of the alloy increases. The main wear mechanism of HEA samples in the temperature range from RT to 400°C was oxidative wear, accompanied by abrasive wear and delamination.

CONFLICT OF INTEREST

The authors declare that they have no conflict of interest.

ACKNOWLEDGEMENTS

The authors appreciate the financial support of the National Key R&D Program of China (2018YFB1106700), the Innovative Research Team Development Program of Ministry of Education of China (IRT_17R83) and the State Key Laboratory of Materials Processing and Die & Mould Technology, Huazhong University of Science and Technology (P2021-018).

REFERENCES

1. B. Cantor, I.T.H. Chang, P. Knight, and A.J.B. Vincent, *Mater. Sci. Eng. A* 375–377, 213 <https://doi.org/10.1016/j.msea.2003.10.257> (2004).
2. J.-W. Yeh, S.-K. Chen, S.-J. Lin, J.-Y. Gan, T.-S. Chin, T.-T. Shun, C.-H. Tsau, and S.Y. Chang, *Adv. Eng. Mater.* 6, 299 <https://doi.org/10.1002/adem.200300567> (2004).
3. B. Gludovatz, A. Hohenwarter, D. Catoor, E.H. Chang, E.P. George, and R.O. Ritchie, *Science* 345, 1153 <https://doi.org/10.1126/science.1254581> (2014).
4. Y. Zhang, T.T. Zuo, Z. Tang, M.C. Gao, K.A. Dahmen, P.K. Liaw, and Z.P. Lu, *Prog. Mater. Sci.* 61, 1 <https://doi.org/10.1016/j.pmatsci.2013.10.001> (2014).
5. D.B. Miracle, and O.N. Senkov, *Acta Mater.* 122, 448 <https://doi.org/10.1016/j.actamat.2016.08.081> (2017).
6. Q.F. He, Z.Y. Ding, Y.F. Ye, and Y. Yang, *JOM* 69, 2092 <https://doi.org/10.1007/s11837-017-2452-1> (2017).
7. F. Wang, Y. Zhang, G. Chen, and H.A. Davies, *Int. J. Mod. Phys. B* 23, 1254 <https://doi.org/10.1142/S0217979209060774> (2009).
8. J.Y. He, W.H. Liu, H. Wang, Y. Wu, X.J. Liu, T.G. Nieh, and Z.P. Lu, *Acta Mater.* 62, 105 <https://doi.org/10.1016/j.actamat.2013.09.037> (2014).
9. K.M. Youssef, A.J. Zaddach, C. Niu, D.L. Irving, and C.C. Koch, *Mater. Res. Lett.* 3, 95 <https://doi.org/10.1080/21663831.2014.985855> (2014).
10. S.G. Ma, S.F. Zhang, J.W. Qiao, Z.H. Wang, M.C. Gao, Z.M. Jiao, H.J. Yang, and Y. Zhang, *Intermetallics* 54, 104 <https://doi.org/10.1016/j.intermet.2014.05.018> (2014).
11. F. Otto, A. Dlouhy, C. Somsen, H. Bei, G. Eggler, and E.P. George, *Acta Mater.* 61, 5743 <https://doi.org/10.1016/j.actamat.2013.06.018> (2013).
12. M.H. Chuang, M.H. Tsai, W.R. Wang, S.J. Lin, and J.W. Yeh, *Acta Mater.* 59, 6308 <https://doi.org/10.1016/j.actamat.2011.06.041> (2011).
13. J. Joseph, N. Haghdadi, K. Shamlaye, P. Hodgson, M. Barnett, and D. Fabijanic, *Wear* 428–429, 32 <https://doi.org/10.1016/j.wear.2019.03.002> (2019).
14. Y. Shi, B. Yang, X. Xie, J. Brechtel, K.A. Dahmend, and P.K. Liaw, *Corros. Sci.* 119, 33 <https://doi.org/10.1016/j.corsci.2017.02.019> (2017).
15. Y. Lu, Y. Dong, S. Guo, L. Jiang, H. Kang, T. Wang, B. Wen, Z. Wang, J. Jie, Z. Cao, H. Ruan, and T. Li, *Sci. Rep.* 4, 6200 <https://doi.org/10.1038/srep06200> (2014).
16. W. Huo, H. Zhou, F. Fang, X. Zhou, Z. Xie, and J. Jiang, *J. Alloys Compd.* 735, 897 <https://doi.org/10.1016/j.jallcom.2017.11.075> (2018).
17. Q. Wu, Z. Wang, T. Zheng, D. Chen, Z. Yang, J. Li, J.J. Kai, and J. Wang, *Mater. Lett.* 253, 268 <https://doi.org/10.1016/j.matlet.2019.06.067> (2019).
18. H. Jiang, D. Qiao, Y. Lu, Z. Ren, Z. Cao, T. Wang, and T. Li, *Scripta Mater.* 165, 145 <https://doi.org/10.1016/j.scriptamat.2019.02.035> (2019).
19. Z. Li, K.G. Pradeep, Y. Deng, D. Raabe, and C.C. Tasan, *Nature* 534, 227 <https://doi.org/10.1038/nature17981> (2016).

20. S. Basu, Z. Li, K.G. Pradeep, and D. Raabe, *Front. Mater.* 5, 30 <https://doi.org/10.3389/fmats.2018.00030> (2018).
21. I.S. Wani, T. Bhattacharjee, S. Sheikh, Y.P. Lu, S. Chatterjee, P.P. Bhattacharjee, S. Guo, and N. Tsuji, *Mater. Res. Lett.* 4, 174 <https://doi.org/10.1080/21663831.2016.1160451> (2016).
22. R. Li, Z. Ren, Y. Wu, Z. He, P.K. Liaw, J. Ren, and Y. Zhang, *Mater. Sci. Eng. A* 802, 140637 <https://doi.org/10.1016/j.msea.2020.140637> (2021).
23. Z. Qiu, C. Yao, K. Feng, Z. Li, and P.K. Chu, *Int. J. Lightweight Mater. Manuf.* 1, 33 <https://doi.org/10.1016/j.ijlmm.2018.02.001> (2018).
24. Z. Tong, X. Ren, J. Jiao, W. Zhou, Y. Ren, Y. Ye, E.A. Larson, and J. Gu, *J. Alloys Compd.* 785, 1144 <https://doi.org/10.1016/j.jallcom.2019.01.213> (2019).
25. S. Xiang, H. Luan, J. Wu, K.F. Yao, J. Li, X. Liu, Y. Tian, W. Mao, H. Bai, G. Le, and Q. Li, *J. Alloys Compd.* 773, 387 <https://doi.org/10.1016/j.jallcom.2018.09.235> (2019).
26. V.R. Molina, A. Weisheit, S. Gein, U. Hecht, and D. Vogiatzief, *Front. Mater.* 7, 275 <https://doi.org/10.3389/fmats.2020.00275> (2020).
27. L. Huang, Y. Sun, A. Amar, C. Wu, X. Liu, G. Le, X. Wang, J. Wu, K. Li, C. Jiang, and J. Li, *Vacuum* 183, 109875 <https://doi.org/10.1016/j.vacuum.2020.109875> (2021).
28. P. Niu, R. Li, Z. Fan, T. Yuan, and Z. Zhang, *Mater. Sci. Eng. A* 814, 141264 <https://doi.org/10.1016/j.msea.2021.141264> (2021).
29. J.Y. Aguilar-Hurtado, A. Vargas-Uscategui, K. Paredes-Gil, R. Palma-Hillerns, M.J. Tobar, and J.M. Amado, *Appl. Surf. Sci.* 515, 146084 <https://doi.org/10.1016/j.apsusc.2020.146084> (2020).
30. X. Liu, L. Zhang, and Y. Xu, *Appl. Phys.* 123, 567 <https://doi.org/10.1007/s00339-017-1151-7> (2017).
31. Y. Han, H. Li, H. Feng, K. Li, Y. Tian, and Z. Jiang, *J. Mater. Sci. Technol.* 65, 210 <https://doi.org/10.1016/j.jmst.2020.04.072> (2021).
32. Y. Lv, X. Zhao, T. Shi, L. Bai, J. Chen, and X. Wang, *J. Mater. Sci.* 55, 2239 <https://doi.org/10.1007/s10853-019-04064-9> (2020).
33. Z. Li, C.C. Tasan, H. Springer, B. Gault, and D. Raabe, *Sci. Rep.* 7, 40704 <https://doi.org/10.1038/srep40704> (2017).
34. P. Zhang, S. Wang, Y. Lv, L. Chen, K. Liu, and D. Zhao, *J. Mater. Sci. Technol.* 15, 2145 <https://doi.org/10.1016/j.jmrt.2021.09.018> (2021).
35. K. Kempen, L. Thijs, J. Van Humbeeck, and J.P. Kruth, *Phys. Procedia* 39, 439 <https://doi.org/10.1016/j.phpro.2012.10.059> (2012).
36. D. Manfredi, F. Calignano, M. Krishnan, R. Canali, E.P. Ambrosio, and E. Atzeni, *Materials* 6, 856 <https://doi.org/10.3390/ma6030856> (2013).
37. T.B. Sercombe, and X. Li, *Mater. Tech.* 31, 77 <https://doi.org/10.1179/1753555715Y.0000000078> (2016).
38. K.G. Prashanth, S. Scudino, H.J. Klauss, K.B. Surreddi, L. Lober, Z. Wang, A.K. Chaubey, U. Kuhn, and J. Eckert, *Mater. Sci. Eng. A* 590, 153 <https://doi.org/10.1016/j.msea.2013.10.023> (2014).
39. X.J. Wang, L.C. Zhang, M.H. Fang, and T.B. Sercombe, *Mater. Sci. Eng. A* 597, 370 <https://doi.org/10.1016/j.msea.2014.01.012> (2014).
40. Z. Zeng, N. Stanford, C.H.J. Davies, J.F. Nie, and N. Birbilis, *Int. Mater. Rev.* 64, 27 <https://doi.org/10.1080/09506608.2017.1421439> (2018).
41. T. Nakata, T. Mezaki, R. Ajima, C. Xu, K. Oh-ishi, K. Shimizu, S. Hanaki, T.T. Sasaki, K. Hono, and S. Kamado, *Scripta Mater.* 101, 28 <https://doi.org/10.1016/j.scriptamat.2015.01.010> (2015).
42. J. Guo, Y. Zhou, C. Liu, Q. Wu, X. Chen, and J. Lu, *Materials* 9, 823 <https://doi.org/10.3390/ma9100823> (2016).
43. G. Chahine, M. Koike, T. Okabe, P. Smith, and R. Kovacevic, *JOM* 60, 50 <https://doi.org/10.1007/s11837-008-0148-2> (2008).
44. B. Vrancken, L. Thijs, J.P. Kruth, and J.V. Humbeeck, *J. Alloys Compd.* 541, 177 <https://doi.org/10.1016/j.jallcom.2012.07.022> (2012).
45. S.S. Al-Bermani, M.L. Blackmore, W. Zhang, and I. Todd, *Metall. Mater. Trans. A* 41, 3422 <https://doi.org/10.1007/s11661-010-0397-x> (2010).
46. T. Scharowsky, V. Juechter, R.F. Singer, and C. Korner, *Adv. Eng. Mater.* 17, 1573 <https://doi.org/10.1002/adem.201400542> (2015).
47. L.C. Zhang, D. Klemm, J. Eckert, Y.L. Hao, and T.B. Sercombe, *Scripta Mater.* 65, 21 <https://doi.org/10.1016/j.scriptamat.2011.03.024> (2011).
48. Y. Zhang, J. Li, X. Wang, Y. Lu, Y. Zhou, and X. Sun, *J. Mater. Sci. Tech.* 35, 902 <https://doi.org/10.1016/j.jmst.2018.09.067> (2019).
49. S. Luo, C. Zhao, Y. Su, Q. Liu, and Z. Wang, *Addit. Manuf.* 31, 100925 <https://doi.org/10.1016/j.addma.2019.100925> (2020).
50. R. Li, P. Niu, T. Yuan, P. Cao, C. Chen, and K. Zhou, *J. Alloys Compd.* 746, 125 <https://doi.org/10.1016/j.jallcom.2018.02.298> (2018).
51. Y. Chew, G.J. Bi, Z.G. Zhu, F.L. Ng, F. Weng, S.B. Liu, S.M.L. Nai, and B.Y. Lee, *Mater. Sci. Eng. A* 744, 137 <https://doi.org/10.1016/j.msea.2018.12.005> (2019).
52. T. Dursun, and C. Soutis, *Mater. Des.* 56, 862 <https://doi.org/10.1016/j.matdes.2013.12.002> (2014).
53. M.K. Kulekci, *Int. J. Adv. Manuf. Technol.* 38, 851 <https://doi.org/10.1007/s00170-007-1279-2> (2008).
54. L.C. Zhang, and L.Y. Chen, *Adv. Eng. Mater.* 21, 1801215 <https://doi.org/10.1002/adem.201801215> (2019).
55. Z. Li, C.C. Tasan, K.G. Pradeep, and D. Raabe, *Acta Mater.* 131, 323 <https://doi.org/10.1016/j.actamat.2017.03.069> (2017).
56. J. Su, D. Raabe, and Z. Li, *Acta Mater.* 163, 40–54 <https://doi.org/10.1016/j.actamat.2018.10.017> (2019).
57. J.A. Spittle, *Int. Mater. Rev.* 51, 247 <https://doi.org/10.1179/174328006X102493> (2006).
58. M.M. Kirka, P. Nandwana, Y. Lee, and R.R. Dehoff, *Scripta Mater.* 135, 130 <https://doi.org/10.1016/j.scriptamat.2017.01.005> (2017).
59. S. Bontha, N.W. Klingbeil, P.A. Kobryn, and H.L. Fraser, *J. Mater. Process. Technol.* 178, 135 <https://doi.org/10.1016/j.jmatprotec.2006.03.155> (2006).
60. S. Allain, J.P. Chateau, O. Bouaziz, S. Migot, and N. Guelton, *Mater. Sci. Eng. A* 387–389, 158 <https://doi.org/10.1016/j.msea.2004.01.059> (2004).
61. J.R.C. Guimaraes, and P.R. Rios, *J. Mater. Sci.* 45, 1074 <https://doi.org/10.1007/s10853-009-4044-0> (2010).
62. X. Zhao, Z. Xue, W. Chen, Y. Wang, and T. Mu, *ChemSuschem* 13, 2038 <https://doi.org/10.1002/cssc.202000173> (2020).
63. Y.Q. Gao, X.Y. Liu, and G.W. Yang, *Nanoscale* 8, 5015 <https://doi.org/10.1039/c5nr08989a> (2016).
64. S. Ma, L. Sun, L. Cong, X. Gao, C. Yao, X. Guo, L. Tai, P. Mei, Y. Zeng, H. Xie, and R. Wang, *J. Phys. Chem. C* 117, 25890 <https://doi.org/10.1021/jp407576q> (2013).
65. Q. Jiang, R. Lu, J. Gu, L. Zhang, K. Liu, M. Huang, P. Liu, S. Zuo, Y. Wang, Y. Zhao, P. Ma, and Z. Fu, *Chem. Eng. J.* 453, 139510 <https://doi.org/10.1016/j.cej.2022.139510> (2023).
66. Y. Yang, L. Dang, M.J. Shearer, H. Sheng, W. Li, J. Chen, P. Xiao, Y. Zhang, R.J. Hamers, and S. Jin, *Adv. Energy Mater.* 8, 1703189 <https://doi.org/10.1002/aenm.201703189> (2018).

Publisher's Note Springer Nature remains neutral with regard to jurisdictional claims in published maps and institutional affiliations.

Springer Nature or its licensor (e.g. a society or other partner) holds exclusive rights to this article under a publishing agreement with the author(s) or other rightsholder(s); author self-archiving of the accepted manuscript version of this article is solely governed by the terms of such publishing agreement and applicable law.